Preclinical ^{89}Zr Immuno-PET of High-Grade Serous Ovarian Cancer and Lymph Node Metastasis

Sai Kiran Sharma[1,2], Kuntal K. Sevak[1], Sebastien Monette[3], Sean D. Carlin[1], James C. Knight[2], Frank R. Wuest[2], Evis Sala[4], Brian M. Zeglis[5], and Jason S. Lewis[1]

[1]Department of Radiology and the Molecular Pharmacology Program, Memorial Sloan Kettering Cancer Center, New York, New York; [2]Department of Oncology, University of Alberta, Edmonton, Alberta, Canada; [3]Tri-Institutional Laboratory of Comparative Pathology, Memorial Sloan Kettering Cancer Center, Weill Cornell Medical College, and The Rockefeller University, New York, New York; [4]Department of Radiology, Memorial Sloan Kettering Cancer Center, New York, New York; and [5]Department of Chemistry, Hunter College and the Graduate Center of the City University of New York, New York, New York

The elevation of cancer antigen 125 (CA125) levels in the serum of asymptomatic patients precedes the radiologic detection of high-grade serous ovarian cancer by at least 2 mo and the final clinical diagnosis by 5 mo. PET imaging of CA125 expression by ovarian cancer cells may enhance the evaluation of the extent of disease and provide a roadmap to surgery as well as detect recurrence and metastases. **Methods:** ^{89}Zr-labeled mAb-B43.13 was synthesized to target CA125 and evaluated via PET imaging and biodistribution studies in mice bearing OVCAR3 human ovarian adenocarcinoma xenografts. Ex vivo analysis of tumors and lymph nodes was performed via autoradiography, histopathology, and immunohistochemistry. **Results:** PET imaging using ^{89}Zr-DFO-mAb-B43.13 (DFO is desferrioxamine) clearly delineated CA125-positive OVCAR3 xenografts as early as 24 h after the administration of the radioimmunoconjugate. Biodistribution studies revealed accretion of ^{89}Zr-DFO-mAb-B43.13 in the OVCAR3 tumors, ultimately reaching 22.3 ± 6.3 percentage injected dose per gram (%ID/g) at 72 h after injection. Most interestingly, activity concentrations greater than 50 %ID/g were observed in the ipsilateral lymph nodes of the xenograft-bearing mice. Histopathologic analysis of the immuno-PET–positive lymph nodes revealed the presence of grossly metastasized ovarian cancer cells within the lymphoid tissues. In control experiments, only low-level, non-specific uptake of ^{89}Zr-labeled isotype IgG was observed in OVCAR3 tumors; similarly, low-activity concentrations of ^{89}Zr-DFO-mAb-B43.13 accumulated in CA125-negative SKOV3 tumors. **Conclusion:** Immuno-PET with ^{89}Zr-labeled mAb-B43.13 is a potential strategy for the noninvasive delineation of extent of disease and may add value in treatment planning and treatment monitoring of high-grade serous ovarian cancer.

Key Words: CA125; ^{89}Zr; positron emission tomography; ovarian cancer

J Nucl Med 2016; 57:771–776
DOI: 10.2967/jnumed.115.167072

Ovarian cancer is the most lethal gynecologic malignancy and the fifth leading cause of cancer-related deaths in women within the United States (*1*). Because of the vague symptomatic progression of the disease, most patients present at advanced stages (III–IV) and often recur after primary cytoreductive surgery and platinum-based chemotherapy, yielding a dismal 5-y survival rate of 27% (*1,2*). High-grade serous ovarian cancer (HGSOC) comprises the major malignant histotype (70%) of epithelial ovarian cancers and bears a molecular signature in the overexpression of MUC16/cancer antigen 125 (CA125), a serum biomarker for ovarian cancer (*3*). Indeed, among epithelial ovarian cancers, the frequency of CA125 positivity is higher in serous histotypes than in mucinous or clear cell disease (*4*).

In recurrent HGSOC, the elevation in serum CA125 levels precedes radiologic detection by 3 mo and predates the clinical presentation of symptoms and diagnosis by a median lag time of 5 mo (*3*). However, elevated serum CA125 levels alone do not qualify as a criterion to initiate treatment in the absence of radiologic evidence of recurrent disease. Ten percent of HGSOCs are reported to be biochemically silent (i.e., have normal serum CA125 levels), and 50% of patients with normal serum CA125 levels at the completion of chemotherapy are found to have active small-volume disease during second-look surgery (*5,6*). At present, serum CA125 levels are quantified via immunoassays, which are often limited in their sensitivity and capability to provide information regarding the rate of antigen shedding and tumor growth in vivo (*7*).

To complicate matters further, metastatic ovarian cancer cells are prone to spread to other parts of the body through the lymphatic system (*8*). To wit, lymph node (LN) involvement in HGSOC patients is observed in up to 25% of cases of early-stage disease (I–II) and 75% of cases of late-stage disease (III–IV) (*9,10*). Interestingly, the frequency of LN metastases at recurrence is found to be higher, even in patients with complete pathologic response to chemotherapy (9). Not surprisingly, the degree of LN involvement strongly influences clinical care decisions: for example, stage I patients with metastatic LNs get upstaged to stage IIIC (*11,12*). Thus, the accurate evaluation of the site and status of LN involvement in addition to peritoneal carcinomatosis is critical for the treatment planning of HGSOC patients (*13*).

In light of the limitations of CA125 as a serum biomarker and the importance of LN involvement in HGSOC, we propose that a method for the noninvasive visualization of CA125 expression by neoplastic cells could provide a valuable clinical tool for the initial

Received Sep. 21, 2015; revision accepted Jan. 7, 2016.
For correspondence or reprints contact: Brian M. Zeglis, Department of Chemistry, Hunter College and the Graduate Center of the City University of New York, New York, NY 10021.
E-mail: bz102@hunter.cuny.edu
Jason S. Lewis, Department of Radiology, 1275 York Ave., Memorial Sloan Kettering Cancer Center, New York, NY 10065.
E-mail: lewisj2@mskcc.org
Published online Feb. 2, 2016.

mapping of the disease as well as for treatment planning and treatment monitoring of recurrent disease. Such a methodology could bridge the gap between the observation of elevated serum CA125 levels and the subsequent radiologic detection of the disease.

In the investigation at hand, we have leveraged our experience with in vivo targeting of CA125 and developed an immuno-PET probe for the molecular imaging of HGSOC (*14*). We have synthesized a ^{89}Zr-labeled variant of the B43.13 antibody—^{89}Zr-DFO-mAb-B43.13 (DFO is desferrioxamine)—that targets CA125 with high affinity (K_D = 1.2 nM) and have evaluated the radioimmunoconjugate in murine models of HGSOC. In doing so, we have created a theranostic variant of mAb B43.13, an antibody previously used for the immunotherapy of ovarian cancer (*15,16*). The ability of ^{89}Zr-DFO-mAb-B43.13 to track LN metastases of HGSOC via PET is a highlight of this study. To the best of our knowledge, this is the first report of a CA125-targeting ^{89}Zr-labeled antibody for the noninvasive visualization of HGSOC.

MATERIALS AND METHODS

PET Imaging

PET imaging experiments were conducted on a microPET Focus rodent scanner (Concorde Microsystems). Mice bearing subcutaneous OVCAR3 (right shoulder) xenografts (150–200 mm^3) were administered ^{89}Zr-DFO-mAb-B43.13 (10.2–12.0 MBq in 200 μL of 0.9% sterile saline, 40–50 μg) via intravenous tail injection (t = 0). Approximately 5 min before PET imaging, mice were anesthetized by inhalation of a 2% isoflurane (Baxter Healthcare)/oxygen gas mixture and placed on the scanner bed; anesthesia was maintained using a 1% isoflurane/gas mixture. PET data for each mouse were recorded via static scans at time points between 24 and 120 h. Images were analyzed using ASIPro VM software (Concorde Microsystems).

Statistical Analysis

All data are expressed as mean ± SEM. Where applicable, statistical differences were analyzed by an unpaired Student *t* test using GraphPad Prism 6 software (GraphPad Software). Comparisons with *P* values of less than 0.05 were considered significant.

RESULTS

Synthesis and Characterization

mAb-B43.13 was conjugated to DFO using *p*-SCN-Bn-DFO and subsequently radiolabeled with $^{89}Zr^{4+}$ to yield ^{89}Zr-DFO-mAb-B43.13 in greater than 99% radiochemical purity and with a specific activity of 203.5 ± 29.6 MBq/mg (5.5 ± 0.8 mCi/mg) (Supplemental Figs. 1 and 2; supplemental materials are available at http://jnm.snmjournals.org). In vitro immunoreactivity experiments using CA125-expressing OVCAR3 epithelial ovarian cancer cells revealed an average immunoreactive fraction of approximately 0.92, and in vitro serum stability assays demonstrated that ^{89}Zr-DFO-mAb-B43.13 is greater than 96% stable to decomposition over 7 d at 37 °C in human serum (Supplemental Figs. 3–5).

PET Imaging and Acute Biodistribution Experiments

Small-animal PET imaging experiments facilitated the visualization of the in vivo performance of ^{89}Zr-DFO-mAb-B43.13. In preliminary experiments, mice (*n* = 5) bearing bilateral OVCAR3 (CA125-positive) and SKOV3 (CA125-negative) ovarian cancer xenografts were administered ^{89}Zr-DFO-mAb-B43.13 (10.2–12.0 MBq) intravenously and subsequently imaged daily from 24–120 h after injection. The images clearly illustrate the selective targeting of ^{89}Zr-DFO-mAb-B43.13 to the CA125-expressing OVCAR3 tumors, with high levels of the radioimmunoconjugate accumulating in the antigen-bearing tissue. In contrast, the CA125-negative SKOV3 tumors were characterized by a low uptake of the tracer, likely due to the non-specific enhanced permeability and retention effect (Fig. 1) (*17*). In subsequent experiments, mice (*n* = 4) bearing subcutaneous OVCAR3 tumors alone were injected with ^{89}Zr-DFO-mAb-B43.13 (10.2–12.0 MBq), and serial PET images were acquired from 24–120 h after injection. These images revealed the clear delineation of the CA125-positive OVCAR3 xenografts, even at early time points (i.e., 24 h; Fig. 2).

These imaging observations were confirmed by biodistribution experiments. To this end, mice bearing subcutaneous OVCAR3 ovarian cancer xenografts (*n* = 4 per group) were injected intravenously with ^{89}Zr-DFO-mAb-B43.13 (0.55–0.74 MBq, 4–6 μg) and euthanized at 24, 48, 72, 96, and 120 h after injection, followed by the collection and weighing of tissues and the assay of ^{89}Zr activity in each tissue (Fig. 3; Supplemental Tables 1 and 2). The amount of radioactivity in the tumor was initially modest (7.2 ± 0.3 percentage injected dose per gram [%ID/g] at 24 h after injection) but increased significantly over the course of the experiment, reaching a maximum of 24.7 ± 7.5 %ID/g at 120 h after injection. As is typical for radioimmunoconjugates, a concomitant decrease in the activity concentration in the blood was also observed, falling to 4.0 ± 3.0 %ID/g at 120 h. The nontarget organ with the highest activity concentration was the liver, with approximately 15 %ID/g at all time points. All other organs—including the ovaries—displayed activity concentrations of less than 5 %ID/g. As a control, an additional cohort of mice (*n* = 4) was coinjected with 480 μg of unlabeled DFO-mAb-B43.13 to selectively saturate the antigen in vivo. Critically, the blocking experiment lowered the uptake of the radioimmunoconjugate in the tumor from 22.3 ± 6.3 to 7.6 ± 3.2 %ID/g (*P* = 0.0093) at 72 h after injection, clearly indicating that ^{89}Zr-DFO-mAb-B43.13 specifically targets the CA125 antigen.

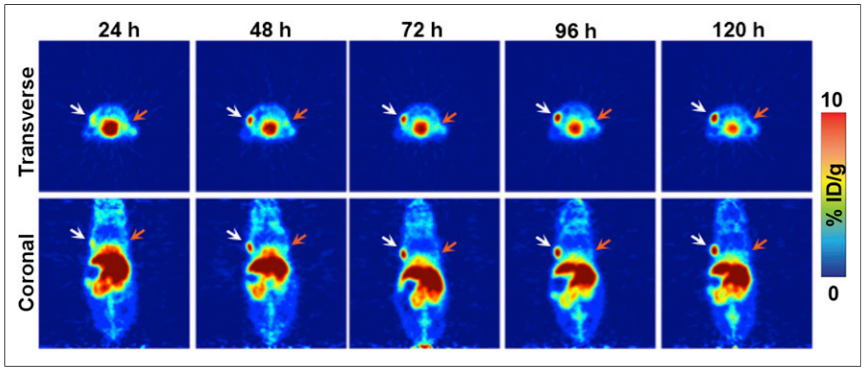

FIGURE 1. Small-animal PET imaging in a bilateral ovarian tumor model. Representative longitudinal transverse and coronal PET images of ^{89}Zr-DFO-mAb-B43.13 (7–10 MBq injected via tail vein) in athymic nude mice bearing bilateral subcutaneous CA125-positive OVCAR3 tumors xenografted on the left shoulder (white arrows) and CA125-negative SKOV3 tumors on the right shoulder (orange arrows).

LN Involvement

The most intriguing facet of the PET images collected using ^{89}Zr-DFO-mAb-B43.13

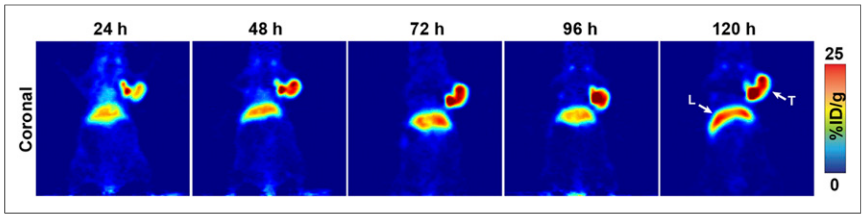

FIGURE 2. CA125-targeted PET imaging with ^{89}Zr-DFO-mAb-B43.13. Serial PET images of an athymic nude mouse bearing a CA125-positive OVCAR3 xenograft after the administration of ^{89}Zr-DFO-mAb-B43.13 via tail vein injection (10.2–12.0 MBq). Coronal planar images intersect the middle of the tumor. L = liver; T = tumor.

was the observation of high activity concentrations in the ipsilateral LNs. In all cases, high levels of uptake were observed in the axillary and brachial LNs proximal to the OVCAR3 xenograft (Figs. 4A and 4B; Supplemental Fig. 6). In a subset of mice, however, an extended LN involvement was observed, with high activity concentrations in the ipsilateral submandibular LN as well (Fig. 4A; Supplemental Fig. 7).

To investigate the uptake of ^{89}Zr-DFO-mAb-B43.13 in the LNs more completely, additional biodistribution studies were performed in athymic nude mice bearing subcutaneous OVCAR3 ovarian cancer xenografts (n = 4 per group). The animals were injected intravenously with ^{89}Zr-DFO-mAb-B43.13 or ^{89}Zr-DFO-IgG (0.5–0.7 MBq; 4–6 μg) and euthanized 72 h after administration of the radioimmunoconjugate. The tissues of interest were collected, weighed, and assayed to determine the amount of activity in each sample. Not surprisingly, the tumoral activity concentrations at 72 h after injection were significantly higher (P = 0.0005) with ^{89}Zr-DFO-mAb-B43.13 (18.1 ± 3.4 %ID/g) than with ^{89}Zr-DFO-IgG (6.1 ± 0.4 %ID/g) (Fig. 4C; Supplemental Table 3). In addition, this study clearly demonstrated high uptake of ^{89}Zr-DFO-mAb-B43.13 in the ipsilateral axillary and brachial LNs, with activity concentrations of 104.8 ± 45.1 and 56.6 ± 39.4 %ID/g, respectively. This is in stark contrast to the level of uptake in the contralateral axillary (3.7 ± 3.2 %ID/g; P = 0.0042) and brachial (6.4 ± 3.7 %ID/g) nodes. For the nonspecific ^{89}Zr-DFO-IgG construct, the degree of uptake of the probe in LNs was drastically reduced (P = 0.0039 in the ipsilateral axillary LNs), and—equally important—no difference in the activity concentrations in the ipsilateral and contralateral nodes was found. PET imaging studies with the isotype control IgG further confirmed these observations (Supplemental Fig. 8). Most interestingly, we observed a progression of LN involvement further up along the ipsilateral chain in some of the OVCAR3 tumor–bearing animals that were serially imaged with ^{89}Zr-DFO-mAb-B43.13 at 3- to 4-wk intervals (Fig. 5; Supplemental Figs. 9–12).

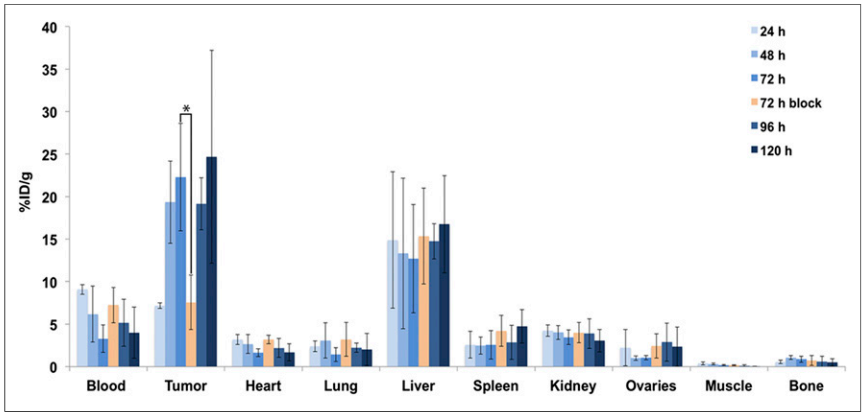

FIGURE 3. Acute biodistribution of ^{89}Zr-DFO-mAb-B43.13 in tumor-bearing mice. Biodistribution data from athymic nude mice (n = 4 per time point) bearing CA125-positive OVCAR3 xenografts after the administration of ^{89}Zr-DFO-mAb-B43.13 via tail vein injection (0.55–0.74 MBq, 4–6 μg). *P = 0.0093. %ID/g values are provided in Supplemental Table 1.

Ex Vivo Analysis

The observation of uptake along the ipsilateral chain of LNs demanded further investigation to confirm the presence for metastatic spread from the primary xenograft. To obtain histopathologic evidence for metastasis, ex vivo analyses of the relevant tissues—the OVCAR3 xenografts as well as the ipsilateral and contralateral axillary, brachial, submandibular, and inguinal LNs—were performed.

Hematoxylin and eosin staining of the frozen tissue sections revealed that the OVCAR3 tumors were positive for the expression of the target CA125 antigen and were well vascularized with few necrotic regions typical of xenografted tumors (Fig. 6A). Digital autoradiography revealed a heterogeneous distribution of ^{89}Zr-DFO-mAb-B43.13 in the tumors (Fig. 6B), with regions of higher uptake closely associated with the tumor vasculature (Fig. 6C). There was no radioactivity in necrotic regions of the tumors, as seen in the lower quartile of the tissue (Fig. 6B).

Histopathologic evaluation of the formalin-fixed tumor sections revealed a multilobulated and invasive neoplasm within disorganized tufts of ovarian cancer cells surrounded by fibrovascular stroma (Fig. 7C; Supplemental Fig. 13). Evaluation of the ipsilateral axillary and brachial LNs revealed metastasis composed of the same cell population as the tumors in all the levels of the tissues examined. Neoplastic cells were also observed multifocally in subcapsular sinuses at all 5 levels. In contrast, the ipsilateral inguinal LNs showed no pathologic changes, whereas the contralateral axillary LNs showed mild medullary sinus edema and erythrophagocytosis but no evidence of metastasis. Immunohistochemical analyses of adjacent sections from the tumors (Fig. 7C) and ipsilateral submandibular (Fig. 7A) and axillary LNs (Fig. 7B) stained positive for CA125, thus reinforcing the presence of grossly metastasized ovarian carcinoma cells.

Critically, the pathologic analysis of the ipsilateral LNs is in excellent agreement with the imaging results. To wit, in mice displaying high-activity concentrations of ^{89}Zr-DFO-mAb-B43.13 in the ipsilateral axillary and brachial nodes but not the ipsilateral submandibular node, it was found that the axillary and brachial nodes showed evidence of metastatic spread whereas the submandibular node did not (Supplemental Fig. 14). In contrast, in mice displaying high-activity concentrations in all 3 ipsilateral

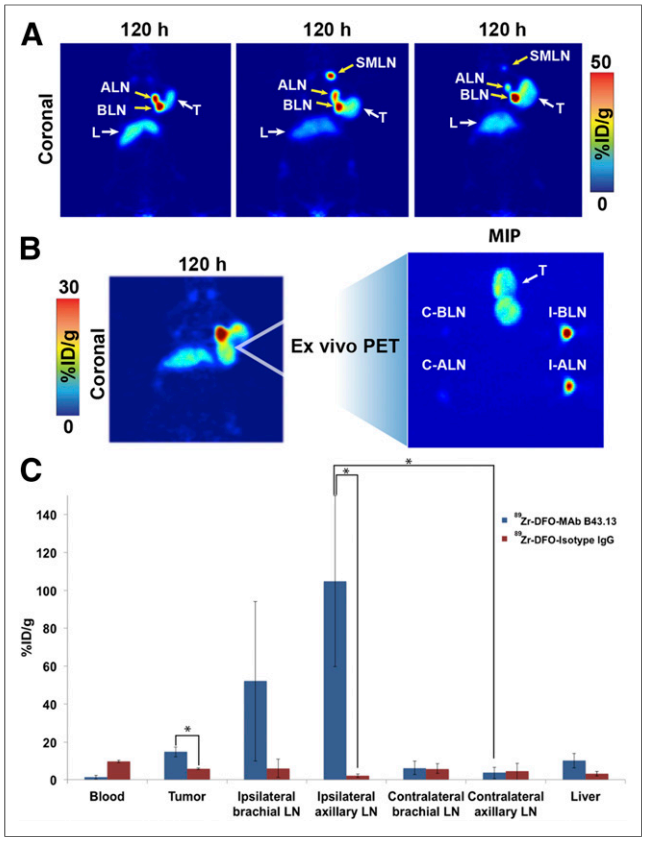

FIGURE 4. Visualization of LNs with ^{89}Zr-DFO-mAb-B43.13. (A) Coronal PET images (120 h after injection) of 3 OVCAR3 tumor–bearing mice demonstrating uptake of the radioimmufnoconjugate in the ipsilateral chain of LNs. (B; left) PET image obtained 120 h after injection of ^{89}Zr-DFO-mAb-B43.13 in an OVCAR3 xenograft–bearing mouse revealing a bilobed tumor with a radioactive focal point indicative of LN involvement. (B; right) Maximum-intensity projection (MIP) from ex vivo PET imaging of the harvested tumor and axillary and brachial LNs from the ipsilateral and contralateral chains. (C) Biodistribution of ^{89}Zr-DFO-mAb-B43.13 and ^{89}Zr-DFO-IgG in OVCAR3 xenograft–bearing mice (n = 4 per group) comparing activity concentrations of the 2 radioimmunoconjugates in the tumor, relevant LNs, and liver. ALN = axillary LNs; BLN = brachial LNs; C-ALN = contralateral axillary LN; C-BLN = contralateral brachial LN; I-ALN = ipsilateral axillary LN; I-BLN = ipsilateral brachial LN; L = liver; SMLN = submandibular LNs; T = tumor. *$P < 0.05$.

LNs, evidence of metastases was found in the ipsilateral submandibular node as well (Fig. 7A), whereas the contralateral submandibular node showed no evidence of metastatic ovarian cancer. Taken together, these data strongly support the reliability and precision of this method for the delineation of LN involvement in our preclinical model of HGSOC.

DISCUSSION

Recent years have played witness to a surge in the use of radioimmunoconjugates for PET imaging of cancer, driven largely by the emergence of ^{89}Zr (half-life = 3.2 d) as a particularly well-suited radioisotope for this application (*18*). In the work at hand, we have extended the potential of immuno-PET to epithelial ovarian cancer by creating a ^{89}Zr-labeled, CA125-targeting radioimmunoconjugate: ^{89}Zr-DFO-mAb-B43.13. This study presents a significant advance from our previous work with a ^{64}Cu-labeled variant of mAb-B43.13, which was limited in its clinical potential due to the short half-life of ^{64}Cu (12.7 h) (*14*). Furthermore, our preclinical data suggest that targeting CA125 via ^{89}Zr-DFO-mAb-B43.13 outperforms ^{18}F-FDG, the radiotracer currently used for clinical PET imaging of ovarian cancer (Supplemental Fig. 15) (*14*).

The biodistribution data are a highlight of this study and provide vital insight into the in vivo behavior of ^{89}Zr-DFO-mAb-B43.13. The uptake of the radioimmunoconjugate in the OVCAR3 xenografts increases steadily over the course of the experiment and is offset by concomitant decreases in the activity in the blood pool and non-target organs. MUC16 is a cell surface glycoprotein, and previous studies using MUC16-targeted antibodies (including mAb-B43.13) have shown slow internalization of the antibody-antigen complex—a finding that may explain the relatively gradual accretion of activity in the OVCAR3 tumors (*14,19*). The persistence of radioactivity in the liver throughout the study may be attributed to the highly perfused nature of the organ or the hepatic clearance of potential high-molecular-weight immunocomplexes of ^{89}Zr-DFO-mAb-B43.13.

The specificity of CA125 targeting by ^{89}Zr-DFO-mAb-B43.13 was established both by imaging experiments using mice bearing bilateral xenografts and by a biodistribution study in which mice bearing OVCAR3 tumors were administered a vast excess of unlabeled DFO-mAb-B43.13 with ^{89}Zr-DFO-mAb-B43.13. In the former, the CA125-positive OVCAR3 xenografts displayed progressively increasing uptake of the radioimmunoconjugate, whereas the CA125-negative SKOV3 tumors showed far lower activity concentrations (Fig. 1). In the latter, a drastic reduction

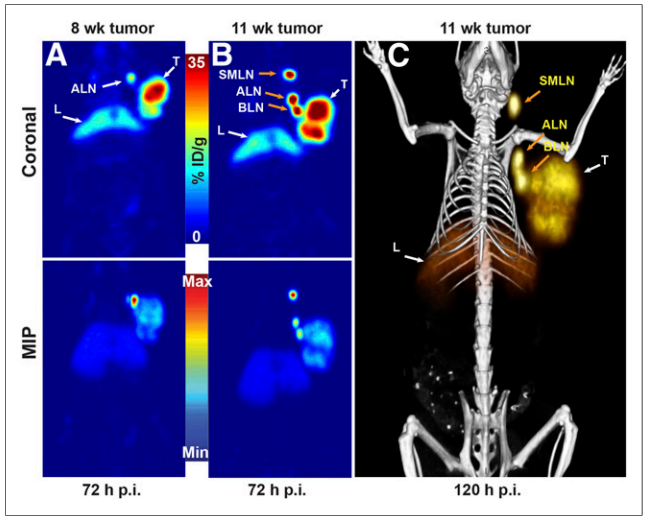

FIGURE 5. PET images of ^{89}Zr-DFO-mAb-B43.13 demonstrating the progression of LN metastasis. (A) Coronal (top) and maximum-intensity projection (MIP; bottom) PET image obtained 72 h after the administration of ^{89}Zr-DFO-mAb-B43.13 to a mouse 8 wk after implantation of an OVCAR3 xenograft on the right shoulder. (B) Coronal (top) and MIP (bottom) PET images obtained 72 h after the administration of ^{89}Zr-DFO-mAb-B43.13 to the same mouse 11 wk after the implantation of the OVCAR3 xenograft on the right shoulder. (C) PET/CT image obtained 120 h after the administration of ^{89}Zr-DFO-mAb-B43.13 to the same mouse 11 wk after the implantation of the OVCAR3 xenograft on the right shoulder. ALN = axillary LNs; BLN = brachial LN; L = liver; max = maximum; min = minimum; p.i. = after injection; SMLN = submandibular LN; T = tumor.

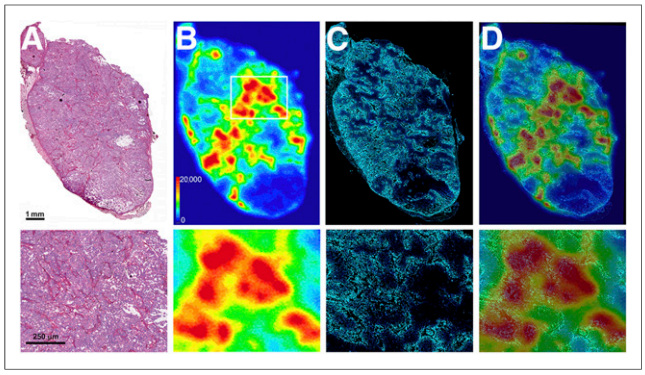

FIGURE 6. Ex vivo analysis of OVCAR3 tumors after PET imaging. (A) Hematoxylin and eosin–stained OVCAR3 tumor section outlining the architecture of the tumor. (B) Digital autoradiograph demonstrating the distribution of ^{89}Zr-DFO-mAb-B43.13 within the tumor. (C) Hoechst 33342 dye (blue) fluorescence map of the tumor vasculature. (D) Overlay of the digital autoradiograph with the Hoechst dye fluorescence map illustrating the role of vasculature in the heterogeneous and limited distribution of ^{89}Zr-DFO-mAb-B43.13 in the tumor. Bottom row contains higher-magnification images of the corresponding sections A–D from the boxed area shown in 6B.

in the activity concentration within OVCAR3 tumors was observed along with a corresponding increase in the activity concentration in the blood, almost certainly resulting from the saturation of the antigen by the unlabeled immunoconjugate (Fig. 3; Supplemental Table 1). In all cases, the CA125-expressing tumor tissue was delineated as early as 24 h after injection, with uptake values that steadily increased thereafter. Indeed, at 72 h after injection ^{89}Zr-DFO-mAb-B43.13 produces images with high contrast and high tumor-to-background ratios. By this time, maximum tumor accretion is achieved with minimal systemic background activity. This would certainly facilitate the visualization of residual and recurrent disease, which is often present as carcinomatous nodules within the peritoneum.

The most intriguing aspect of the PET imaging experiments was the visualization of high concentrations of ^{89}Zr-DFO-mAb-B43.13 in the LNs proximal to the tumor. The specificity of this uptake was confirmed in biodistribution studies that used ^{89}Zr-DFO-IgG as an isotype control. A starkly different biodistribution profile was observed between the 2 radioimmunoconjugates, with ^{89}Zr-DFO-mAb-B43.13 exhibiting far higher activity concentrations in the CA125-positive OVCAR3 xenografts as well as the proximal LNs (Supplemental Table 3).

HGSOC patients commonly present with widespread intraperitoneal disease and LN involvement. The paraaortic region is the prime site for early LN metastasis, followed by pelvic LN involvement (*10,20*). This phenomenon poses a surgical challenge if the disease is present in the LNs above the renal hilum and in the chest, as these nodes are difficult to resect. There are also isolated clinical reports of axillary LN metastasis of HGSOC (*21*). Notably, sentinel LN procedures are generally not performed in the ovarian cancer setting because of the challenge posed by the local spread of the disease within the peritoneum. More recently, the presence of tumor cells in the lumens of the lymphatic capillaries (lymphovascular space invasion) has been identified as an early indicator of nodal metastasis in patients (*22*). In our studies, the high volume of metastatic disease confined within the small and densely packed LNs seemed to be the root cause for the high concentrations of ^{89}Zr-DFO-mAb-B43.13 within the ipsilateral nodes. Most importantly, the selectivity of this effect is illustrated by the correlation between the histopathologic analysis of the nodes and the PET images: the LNs delineated in the PET scans were pathologically confirmed to contain metastatic disease, whereas the LNs not visualized in PET scans proved negative for the presence of ovarian cancer metastasis on histopathologic analysis. In other words: no false-negatives were observed.

In addition to its role as a marker for the peritoneal spread of ovarian cancer, high preoperative serum levels of CA125 also help identify candidates for surgical lymphadenectomy (*8,23*). Despite the shedding of CA125 by OVCAR3 cells in vitro, immunoassays did not reveal detectable levels of the antigen in the serum of tumor-bearing animals (Supplemental Fig. 16B). This may be a limitation of this subcutaneous xenograft model, as we observed the subcutaneous collection of CA125-rich lymphatic fluid surrounding the tumor (Supplemental Figs. 16A and 17). That said, it is also possible that the amount of circulating CA125 in the tumor-bearing mice was below the detection limit of the enzyme-linked immunosorbent assay. Clearly, further investigation of the utility of ^{89}Zr-DFO-mAb-B43.13 in more clinically and pathologically relevant animal models of HGSOC is warranted.

In the interest of balance, it is important to note that despite its promise, ^{89}Zr-DFO-mAb-B43.13 does have some minor limitations. First, the persistence of radioactivity in the liver throughout the investigation may mask the detection of liver metastases and carcinomatous nodules present in its immediate vicinity. However, parenchymal liver metastases are rare at presentation and are more commonly found as surface capsular deposits on recurrence (*24*). Second, CA125 is also expressed in several non-gynecologic malignancies including breast, gastric, and lung cancers and in benign

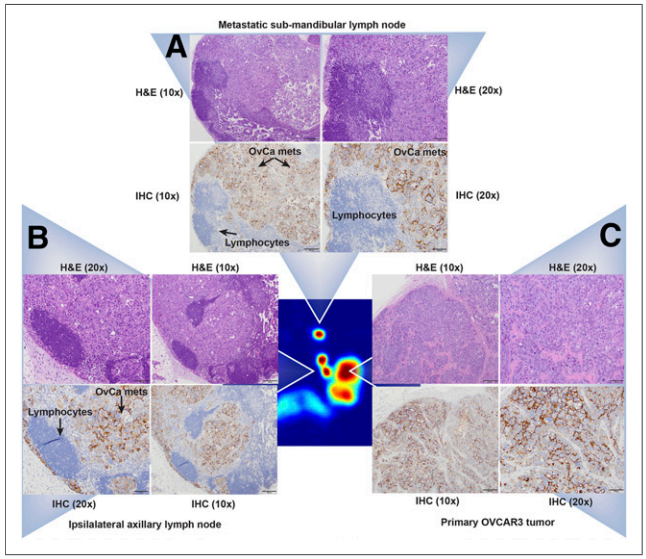

FIGURE 7. Histopathologic analyses of the primary tumor and the ipsilateral submandibular and axillary LN tissues. (Central image) Coronal PET image showing the primary OVCAR3 tumor and the ipsilateral submandibular and axillary LNs in a mouse (Fig. 5B) injected with ^{89}Zr-DFO-mAb-B43.13. (A–C) ×20 and ×10 magnification of tissue sections from the ipsilateral submandibular LN (A), the ipsilateral axillary LN (B), and the primary tumor stained with hematoxylin and eosin (H&E; top) and immunohistochemistry (IHC; bottom) for CA125 (C). In IHC images, the lymphocytes appear blue, whereas the metastatic ovarian cancer cells appear dark brown, indicating positive staining for the expression of CA125 along the circumference of ovarian cancer (OvCa) cells.

conditions such as pregnancy and menstruation and maladies such as endometriosis, liver disease, and congestive heart failure (*16*). Finally, mAb-B43.13 is a murine antibody and thus poses the risk of provoking a human anti-mouse antibody response in patients. However, variants of mAb-B43.13 have already been used in HGSOC patients for radioimmunoscintigraphy and demonstrated a pronounced immunotherapeutic effect (*25*). Nonetheless, the humanization of mAb-B43.13 is currently under way and will undoubtedly increase the potential of ^{89}Zr-DFO-mAb-B43.13 as a clinical immuno-PET probe.

CONCLUSION

The work at hand represents a significant step forward in our efforts toward the development of a CA125-targeted probe for the PET imaging of HGSOC. We strongly believe that ^{89}Zr-DFO-mAb-B43.13 has the potential to create roadmaps for the management of HGSOC by facilitating the selection of patients for surgery and treatment based on the site and status of LN involvement and the extent of the metastatic spread of the disease. Furthermore, ^{89}Zr-DFO-mAb-B43.13 could also prove valuable in the detection of metastases and recurrent disease, both of which affect treatment options and survival outcomes for ovarian cancer patients. Ultimately, we contend that ^{89}Zr-mAb-DFO-B43.13 is particularly well positioned to make a near-term impact on the clinical care of ovarian cancer not only because of the promising results described herein but also because of mAb-B43.13's previous experience in the clinic as well as the growing clinical enthusiasm for ^{89}Zr immuno-PET.

DISCLOSURE

The costs of publication of this article were defrayed in part by the payment of page charges. Therefore, and solely to indicate this fact, this article is hereby marked "advertisement" in accordance with 18 USC section 1734. We gratefully acknowledge the MSKCC Small Animal Imaging Core Facility, which is supported in part by NIH grant P30 CA08748. We also thank the NIH (R00 CA1440138, BMZ), William H. and Alice Goodwin and the Commonwealth Foundation for Cancer Research, the Center for Experimental Therapeutics of Memorial Sloan Kettering Cancer Center, the Natural Sciences and Engineering Research Council of Canada, and the Dianne and Irving Kipnes Foundation. No other potential conflict of interest relevant to this article was reported.

REFERENCES

1. Siegel RL, Miller KD, Jemal A. Cancer statistics, 2015. *CA Cancer J Clin.* 2015; 65:5–29.
2. Gadducci A, Cosio S, Zola P, Landoni F, Maggino T, Sartori E. Surveillance procedures for patients treated for epithelial ovarian cancer: a review of the literature. *Int J Gynecol Cancer.* 2007;17:21–31.
3. Pignata S, Cannella L, Leopardo D, Bruni GS, Facchini G, Pisano C. Follow-up with CA125 after primary therapy of advanced ovarian cancer: in favor of continuing to prescribe CA125 during follow-up. *Ann Oncol.* 2011;22(suppl 8): viii40–viii44.
4. Gupta D, Lis CG. Role of CA125 in predicting ovarian cancer survival: a review of the epidemiological literature. *J Ovarian Res.* 2009;2:13.
5. Nossov V, Amneus M, Su F, et al. The early detection of ovarian cancer: from traditional methods to proteomics—can we really do better than serum CA-125? *Am J Obstet Gynecol.* 2008;199:215–223.
6. Marcus CS, Maxwell GL, Darcy KM, Hamilton CA, McGuire WP. Current approaches and challenges in managing and monitoring treatment response in ovarian cancer. *J Cancer.* 2014;5:25–30.
7. Hori SS, Gambhir SS. Mathematical model identifies blood biomarker-based early cancer detection strategies and limitations. *Sci Transl Med.* 2011;3: 109ra116.
8. Ayhan A, Gultekin M, Dursun P, et al. Metastatic lymph node number in epithelial ovarian carcinoma: does it have any clinical significance? *Gynecol Oncol.* 2008;108:428–432.
9. Di Re F, Baiocchi G. Value of lymph node assessment in ovarian cancer: status of the art at the end of the second millennium. *Int J Gynecol Cancer.* 2000;10:435–442.
10. Takeshima N, Hirai Y, Umayahara K, Fujiwara K, Takizawa K, Hasumi K. Lymph node metastasis in ovarian cancer: difference between serous and nonserous primary tumors. *Gynecol Oncol.* 2005;99:427–431.
11. Onda T, Yoshikawa H, Yasugi T, et al. Patients with ovarian carcinoma upstaged to stage III after systematic lymphadenctomy have similar survival to stage I/II patients and superior survival to other stage III patients. *Cancer.* 1998;83:1555–1560.
12. Berek JS. Lymph node-positive stage IIIC ovarian cancer: a separate entity? *Int J Gynecol Cancer.* 2009;19(suppl 2):S18–S20.
13. Pereira A, Perez-Medina T, Magrina JF, et al. The impact of pelvic retroperitoneal invasion and distant nodal metastases in epithelial ovarian cancer. *Surg Oncol.* 2014;23:40–44.
14. Sharma SK, Wuest M, Wang M, et al. Immuno-PET of epithelial ovarian cancer: harnessing the potential of CA125 for non-invasive imaging. *EJNMMI Res.* 2014;4:60.
15. Berek JS. Immunotherapy of ovarian cancer with antibodies: a focus on oregovomab. *Expert Opin Biol Ther.* 2004;4:1159–1165.
16. Scholler N, Urban N. CA125 in ovarian cancer. *Biomarker Med.* 2007;1:513–523.
17. Heneweer C, Holland JP, Divilov V, Carlin S, Lewis JS. Magnitude of enhanced permeability and retention effect in tumors with different phenotypes: ^{89}Zr-albumin as a model system. *J Nucl Med.* 2011;52:625–633.
18. Deri MA, Zeglis BM, Francesconi LC, Lewis JS. PET imaging with ^{89}Zr: from radiochemistry to the clinic. *Nucl Med Biol.* 2013;40:3–14.
19. Xiao Z, McQuarrie SA, Suresh MR, Mercer JR, Gupta S, Miller GG. A three-step strategy for targeting drug carriers to human ovarian carcinoma cells in vitro. *J Biotechnol.* 2002;94:171–184.
20. Nagano H, Muraoka M, Takagi K. Recurrent ovarian cancer with multiple lymph nodes metastases successfully treated with lymphadenectomy as secondary cytoreductive surgery: a case report. *Int J Surg Case Rep.* 2014;5:412–415.
21. Ceccarelli F, Barberi S, Pontesilli A, Zancla S, Ranieri E. Ovarian carcinoma presenting with axillary lymph node metastasis: a case report. *Eur J Gynaecol Oncol.* 2011;32:237–239.
22. Matsuo K, Sheridan TB, Yoshino K, et al. Significance of lymphovascular space invasion in epithelial ovarian cancer. *Cancer Med.* 2012;1:156–164.
23. Kim HS, Park NH, Chung HH, Kim JW, Song YS, Kang SB. Significance of preoperative serum CA-125 levels in the prediction of lymph node metastasis in epithelial ovarian cancer. *Acta Obstet Gynecol Scand.* 2008;87:1136–1142.
24. Akin O, Sala E, Moskowitz CS, et al. Perihepatic metastases from ovarian cancer: sensitivity and specificity of CT for the detection of metastases with and those without liver parenchymal invasion. *Radiology.* 2008;248:511–517.
25. Madiyalakan R, Sykes TR, Dharampaul S, et al. Antiidiotype induction therapy: evidence for the induction of immune response through the idiotype network in patients with ovarian cancer after administration of anti-CA125 murine monoclonal antibody B43.13. *Hybridoma.* 1995;14:199–203.